Electrically Controlled Photonic Circuits of Field-Induced Dipolaritons with Huge Nonlinearities

Dror Liran and Ronen Rapaport*
Racah Institute of Physics, The Hebrew University of Jerusalem, Jerusalem 9190401, Israel

Jiaqi Hu, Nathanial Lydick, and Hui Deng
University of Michigan, Ann Arbor, Michigan 48109, USA

Loren Pfeiffer
Department of Electrical Engineering, Princeton University, Princeton, New Jersey 08544 USA

(Received 21 October 2023; accepted 3 July 2024; published 8 August 2024)

Electrically controlled photonic circuits hold promise for information technologies with greatly improved energy efficiency and quantum information processing capabilities. However, weak nonlinearity and electrical response of typical photonic materials have been two critical challenges. Therefore, hybrid electronic-photonic systems, such as semiconductor exciton polaritons, have been intensely investigated for their potential to allow higher nonlinearity and electrical control, with limited success so far. Here we demonstrate an electrically gated waveguide architecture for field induced dipolar polaritons that allows enhanced and electrically controllable polariton nonlinearities, enabling an electrically tuned reflecting switch (mirror) and transistor of the dipolar polaritons. The polariton transistor displays blockade and antiblockade by compressing a dilute dipolar-polariton pulse exhibiting very strong dipolar interactions. The large nonlinearities are explained using a simple density-dependent dipolar polarization field that very effectively screens the external electric field. We project that a quantum blockade at the single polariton level is feasible in such a device.

DOI: 10.1103/PhysRevX.14.031022

Subject Areas: Optoelectronics, Photonics, Semiconductor Physics

I. INTRODUCTION

Photons are excellent carriers of information. Bits or qubits can be encoded on their different degrees of freedom, guided in complex on-chip integrated light circuits, and travel macroscopic distances with minimal loss or decoherence [1–3]. Yet photons do not interact with each other nor with external electric and magnetic fields. Therefore it has been a challenge to use them for information processing, such as gates and logic operations, or to integrate them with electronic control and other electronic-based states. Therefore, integrated logic circuits are still mainly made of purely electronic states, either free carriers or new attempts for circuits based on bare excitons [4–7]. These approaches are limited in their operation speed and in their ability to transfer information coherently. A promising route to induce photon-photon interactions is to strongly couple a confined photon with a resonant electronic excitation to create a light-matter superposition state known as a polariton [8–10]. Polaritons can preserve the photonic information while enabling effective photon-photon interactions and interactions with external fields via their matter constituent. In atomic platforms, laser-controlled quantum operations utilizing Rydberg polaritons have been successfully demonstrated [11,12], but on-chip integration or electrical control is very challenging. In semiconductor platforms, microcavity exciton polaritons have been used to demonstrate optically controlled switches [13–15], routers [16,17] and transistors [18–20], as well as a few percent of antibunching [21,22], albeit only through inefficient optical control and only in relatively bulky vertical or free-space microcavities that are still challenging for integration. Moreover, the nonlinearity of these polariton systems, even though much stronger than conventional optical materials, remain limited due to the contact like interactions of polaritons [23–25]. Alternatively, exciton polaritons in waveguide (WG) structures have recently been shown to feature nonlinearities over an order of magnitude greater than their microcavity counterpart [26–28]. In this system, electrical gates can be placed in the proximity of the waveguide to polarize the excitonic component of the polaritons, creating dipolar polaritons, or dipolaritons, which

*Contact author: ronenr@phys.huji.ac.il

interact with each other strongly through the long-range dipole-dipole interactions [26–32]. The waveguide dipolaritons thus hold great promise for constructing electrically controlled complex quantum-light circuitry on chip [33–39], yet no such demonstration has been made.

In this work, we make an important step toward polariton-based quantum circuitry, by using sectioned electrically gated waveguide devices, and demonstrate a reflecting polariton electrical switch and a polariton transistor, operating with a very low number of photons. We first show that fast propagating polaritons in a sectioned gated waveguide device can be very efficiently blocked and reflected by an electrically induced mismatch in the polariton density of states, thus realizing an electrical Stark switch for light. We then show a device that acts as an electrically tuned polariton optical transistor, displaying both a blockade and an anti-blockade for a dilute polariton pulse. The switch and transistor display an exceptional extinction ratio up to > 20 dB. The apparent large nonlinearity of the very dilute polariton pulse is due to a combination of the strong field-induced repulsive dipolar interactions [27], together with a drastic slowdown of the polariton speed under the electrical gate, where the polaritons suddenly become dipolar and excitonlike and are "squeezed" into a high-density, strongly interacting pulse. The strong nonlinearities are explained by an effective field-induced dipolar screening model, elucidating the large interaction enhancement of induced dipolaritons compared to nonpolar polaritons and fixed-length dipolaritons. We project that a true two-polariton blockade is within close reach in such a system.

II. ELECTRICAL SWITCH FOR WAVEGUIDE DIPOLARITONS

Our first device, a split-gate waveguide, illustrated in Fig. 1(a), is designed to realize an electrostatic potential step for the polaritons and to demonstrate an electrically controlled Stark switch for polaritons. The device is fabricated by depositing a 20-μm-wide and 200-μm-long indium-tin-oxide (ITO) strip on top of an AlGaAs slab WG sample containing multiple GaAs quantum wells (QWs) in its core. The full details of the sample, which is similar to the one in our previous works [26,27,34], can be found in the Supplemental Material (SM) [40]. The strong interaction between the heavy-hole exciton X_{hh}, the light-hole exciton X_{lh}, and the transverse-electric (TE) WG photon results in three polariton modes: lower polariton (LP), middle polariton (MP), and an upper polariton [26] (the polariton modes resulting from the transverse magnetic (TM) WG mode, seen in Fig. 1(c), are not discussed in this work). The dispersion relation of the LP and MP along the bare modes (X_{hh}/photon) is plotted on top of measured spectra in Figs. 1(c)–1(e). The ITO strip laterally confines the optical modes [34], and also serves as the top electrode with respect to the doped substrate. In this design, the top ITO electrode is split, and has a 1 μm gap in the middle, and the two resulting sections are independently biased with respect to the common bottom electrode. The vertically aligned electric field [F; see Eq. (A8) in Appendix A] under each section polarizes the exciton constituent of the polariton and results in dipolaritons with electric dipole moments along the z axis [26,27]. The induced dipole moment then interacts with the same electric field resulting in a Stark shift of the exciton, $\Delta E_X(F) = X_{\mathrm{hh}}(F) - X_{\mathrm{hh}}(0) = -\alpha F^2$, where α is the polarizability, as is seen in Fig. 1(b). This Stark shift of the exciton and thus of the whole polariton dispersion as well as the polariton dipole moment can be controlled independently in each section by the corresponding applied bias. The polariton energies hereafter are quoted relative to $X_{\mathrm{hh}}(0) = 1527$ meV as $\tilde{E}(|\beta|) = E(|\beta|) - X_{\mathrm{hh}}(0)$, where β is the WG-polariton propagation wave vector.

A schematic description of an experiment, done at $T \simeq 5$ K, is shown in Fig. 1(a). The WG polaritons are injected to right channel ∼15 μm from the ITO gap, using a nonresonant pulsed laser ($\lambda_p = 774$ nm, pulse duration $\tau_p = 94$ ps, and a repetition rate 200 kHz) and then propagate toward the two ends of the channel and couple out through left and right grating couplers.

Figure 1(c) presents the dispersion of the polaritons emitted from the left and right grating couplers, taken at a flat potential, where $F_L = F_R = 0$. The spectrum shows a similar dispersion and occupation of LPs from the two sides of the channel, as expected from symmetry. It also shows that the gap in the ITO has a negligible effect, and that left-moving LPs do not experience a significant reflection or loss compared to right movers, as they experience a continuous potential landscape and an identical dispersion on both sections, $\tilde{E}_R(|\beta|) = \tilde{E}_L(|\beta|)$.

The situation is modified when a finite F_L is applied to the left section: The left LP and MP modes become red detuned with respect to the right LP and MP modes, creating a dispersion mismatch for the left movers, $\tilde{E}_R(|\beta|) \neq \tilde{E}_L(|\beta|)$. This has an increasingly dramatic effect on the dynamics as seen in Figs. 2(d) and 2(e): While the right movers seem to have a slight increase in population, the transmission of the left movers from the left output coupler becomes much weaker for all energies, with essentially zero transmission for all states above the corresponding bare exciton energy.

This effect is explained qualitatively in the schematics in the middle column of Figs. 1(c)–1(e): While the polariton dispersion at the right section is unchanged, in the left section it becomes increasingly redshifted with increased F_L, and the polaritons become dipolar [27]. As a result, the β mismatch of the LP modes with a given energy in the right and left sections increases, creating an increased discontinuity in $\beta(\tilde{E})$ for the left movers at the intersection between the two sections. This also creates a discontinuity in the polariton group velocity v_g, where polaritons moving to the left section experience a sudden decreased v_g, i.e., a slowdown, in particular for

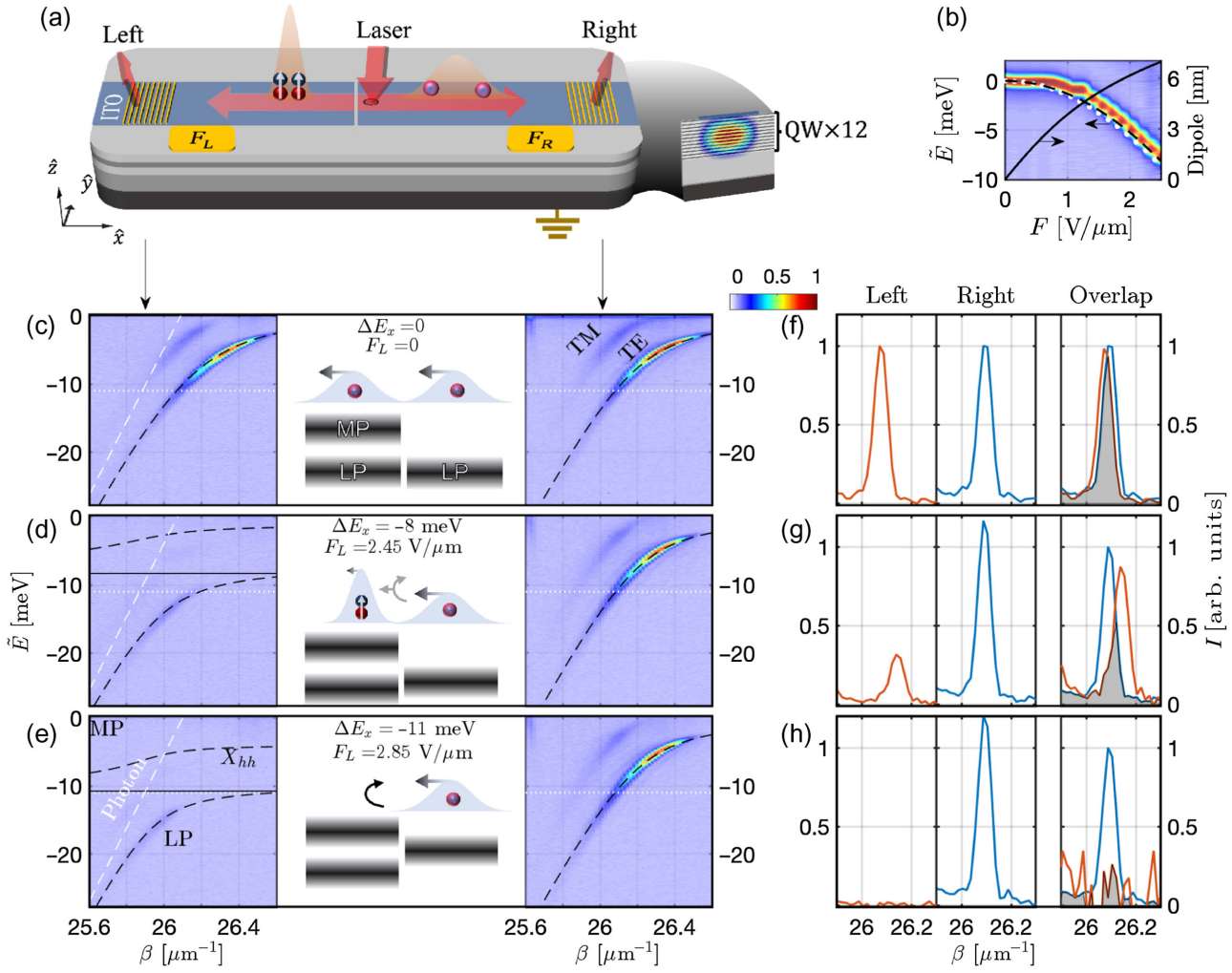

FIG. 1. Electrically polarized polaritons in a split-gate waveguide. (a) Illustration of the device. A slab waveguide with 12 QWs in its core. The ITO strip defines the optical mode laterally and serves as a top electrode. The channel is split, allowing an independent electrical field in each section (F_R/F_L). The polaritons are injected into the center of the channel, propagate to both directions, and couple out through the gratings. (b) The energy of X_{hh} as a function of F. The white dots are the numerically calculated exciton energies (see SM [40]), and the dashed black line is a quadratic fit $\Delta E_X = -\alpha F^2$ with $\alpha = 1.3$ meV/(V^2/μm^2). The black solid line plots the calculated electric dipole length (right-hand axis). (c)–(e) Measured dispersion spectra from the two sides of the channel, for three different values of $\Delta E_X(F_L, F_R = 0)$. The LP and MP fits are plotted with dashed black lines, whereas X_{hh} and the photon are marked by solid black and dashed white lines, respectively. The middle column presents schematics of the step-potential effect. The increase in ΔE_X decreases the overlap of the LP in the two sections, decreasing the transmitted signal, until near blockage. (f)–(h) Cross sections of the spectra, at $\tilde{E}(|\beta|) = -11$ meV, marked in (c)–(e) by dotted white lines. The left-hand (right-hand) side corresponds to the transmission (reflection). The rightmost column shows overlaid, normalized cross-section pairs with gray-filled overlaps.

polaritons with $\tilde{E}_R(|\beta|) \simeq \tilde{E}_X(F_L)$. This discontinuity results in a decreased LP transmission and an increase in reflection. Strikingly, left movers with energies $\tilde{E}_R(|\beta|)$ above $\tilde{E}_X(F_L)$ have no polariton states in the left section, as they lie in the Rabi energy gap between the LP and the MP branches (LP-MP gap), so they experience zero transmission as clearly seen in the left spectra in Figs. 1(d) and 1(e).

In Figs. 1(f)–1(h) we plot a constant energy cross section of normalized emitted intensity from the left and right couplers, $I_{R,L}(\tilde{E} = -11\ \mathrm{meV}, |\beta|)$. The decrease in the transmission and increase in reflection with increasing F_L can be clearly seen, as well as the mismatch in the propagation constants β on both sides. The rightmost column plots the signal from the two sides overlaid, each normalized by its own integral. The relative shift in β and the decrease in the overlap of the two sides (gray filling) is clearly seen. When $\tilde{E}_R(|\beta|)$ lies in the LP-MP gap there is essentially zero overlap and zero transmission, as seen in Fig. 1(h).

Figures 2(a)–2(c) plot the decreasing transmission (T) of 3 different LP energies (integrated over all β), with increasing Stark shift $-\Delta E_X(F_L)$. Remarkably, it agrees

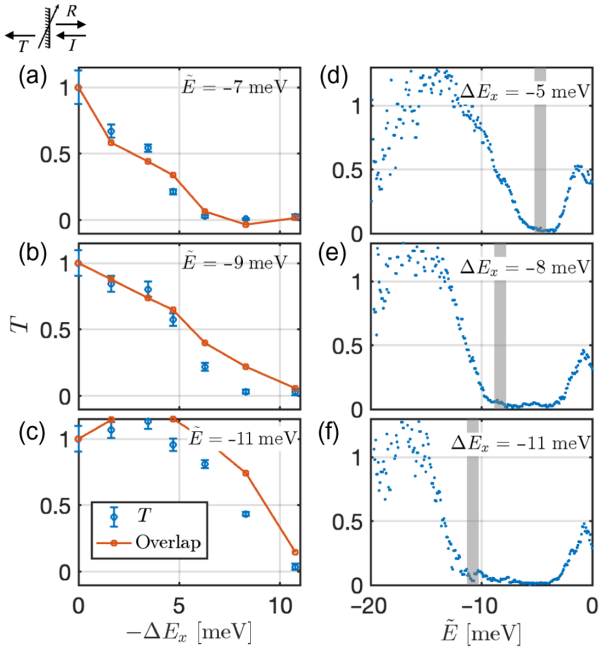

FIG. 2. A tunable polariton electrical mirror with a voltage-controlled potential step. (a)–(c) Transmission of the left-moving polaritons as a function of $-\Delta E_X(F_L)$, for different energy cuts ($\tilde{E} = -7, -9, -11$ meV, respectively). The transmission (blue symbols) is compared against the overlap of the states in the two sides of the potential discontinuity (red dots). The error bars are the standard deviation. (d)–(f) Transmission of the left-moving polaritons for different step size [$\Delta E_X(F_L) = -5, -8, -11$ meV, respectively]. The energy of the exciton is marked by a vertical gray line. The signal at energies near $\tilde{E} = 0$ results from the residual bare exciton emission at the excitation point leaking into the field of view of the collection optics.

well with the measured overlap between the polariton states in both sections, as was plotted in Figs. 1(f)–1(h). This validates that the transmission process through the discontinuity is coherent, conserving energy and momentum.

In Figs. 2(d)–2(f) we present $T(\tilde{E}_R)$ for 3 different values of F_L. An electrically tunable zero transmission gap with a very high extinction ratio is observed, demonstrating that the polariton optical transmission can be selectively tuned in a continuous manner by low-voltage electrical gating, thus facilitating a tunable electro-optical Stark switch for light.

III. ELECTRICALLY CONTROLLED OPTICAL TRANSISTOR FOR DIPOLARITONS

Next, based on the concepts of our first device, we turn to our second device, illustrated in Fig. 3(a), designed to realize an electrically controlled polariton transistor, and to demonstrate a blockade and an antiblockade for a dilute polariton pulse, utilizing enhanced dipolar interactions of ultraslow polaritons. The device, 200 μm long, is divided into three sections: a short 10 μm section positioned 50 μm from the left grating—"the gate"—and its two sides—"the channel." The two channel sections are held at $F_C = 0$ at all times, while a field F_G under the gate creates a local Stark shift of $X_{\mathrm{hh},G}$: $[\Delta E_X = X_{\mathrm{hh}}(F_G) - X_{\mathrm{hh}}(0)]$. Low-density polariton pulses, each containing $N_P \simeq 400$ polaritons (see SM for details [40]) are nonresonantly injected through the right channel section, either 50 or 100 μm away from the gate section, and then propagate in the two directions. Here we consider only left movers that pass through the gate section.

Figure 3(b) presents the dispersion of the polaritons emitted from the left grating for a flat potential $F_G = 0$. This is used as a reference. When the gate is biased, the LP and MP states in the gate are redshifted with respect to those of the channel, as presented in the schematics of Fig. 3(c). This electrically induced discontinuity blocks the dilute pulse of left movers with energies at the middle of the LP-MP gap, $\tilde{E} = -10.5$ meV (see white dashed line), with a maximal extinction ratio > 20 dB, limited only by the measurement SNR. Figure 3(f) plots the transmission for polaritons with $\tilde{E} = -10.5$ meV, as a function of $-\Delta E_X$, again displaying an electrical Stark-switch behavior for the polaritons, but with an even sharper on-off switching field, $\Delta F_G \simeq 0.5$ V/μm, due to the well-type double discontinuity in the effective potential, compared to the step-shaped single discontinuity in the first device. Interestingly, the transmission starts to increase again with a further increase of F_G when the LP in the channel coincide with the MP in the gate. This effect will become of importance later for demonstrating a blockade of dipolaritons.

Figure 3(e) shows the spatially resolved spectrum from the gated device [(with $\Delta E_X(F_G) = -7.5$ meV]. A blocking in the transmission spectrum is also clearly observed at the bottom grating at energies corresponding to the LP-MP energy gap under the biased gate (red double arrow), similar to the first device. This blocking of the transmission through the gate is accompanied by an increase in emission from the right coupler at the corresponding energies (red single arrow), indicating that left movers were at least partially reflected from the gate and became right movers. The bottom of Fig. 3(e) shows the group velocities $v_g^{G,C}(\tilde{E})$ of the polaritons under the gate and the channel, respectively; the group velocity is calculated from the derivative of the polariton energy dispersion with respect to the momentum [Eq. (S15) in SM [40]]. While $v_g^G \simeq v_g^C \simeq v_{\mathrm{ph}}$ at low energies, where the LP are photonlike, there is a growing mismatch at higher energies. Remarkably, at polariton energies approaching the LP-MP gap in the gate, v_g^G dramatically drops toward the bare X_{hh} velocity v_X, resulting in an extreme slowdown of polaritons under the gate, as large as $v_X/v_{\mathrm{ph}} \sim 10^{-4}$. Interestingly, a weak emission from under the gate (at $x \sim -50$ μm) is seen (marked by the double red arrow) at exactly the energy range of these ultraslow dipolaritons. We thus attribute this emission to ultraslow dipolaritons which are effectively

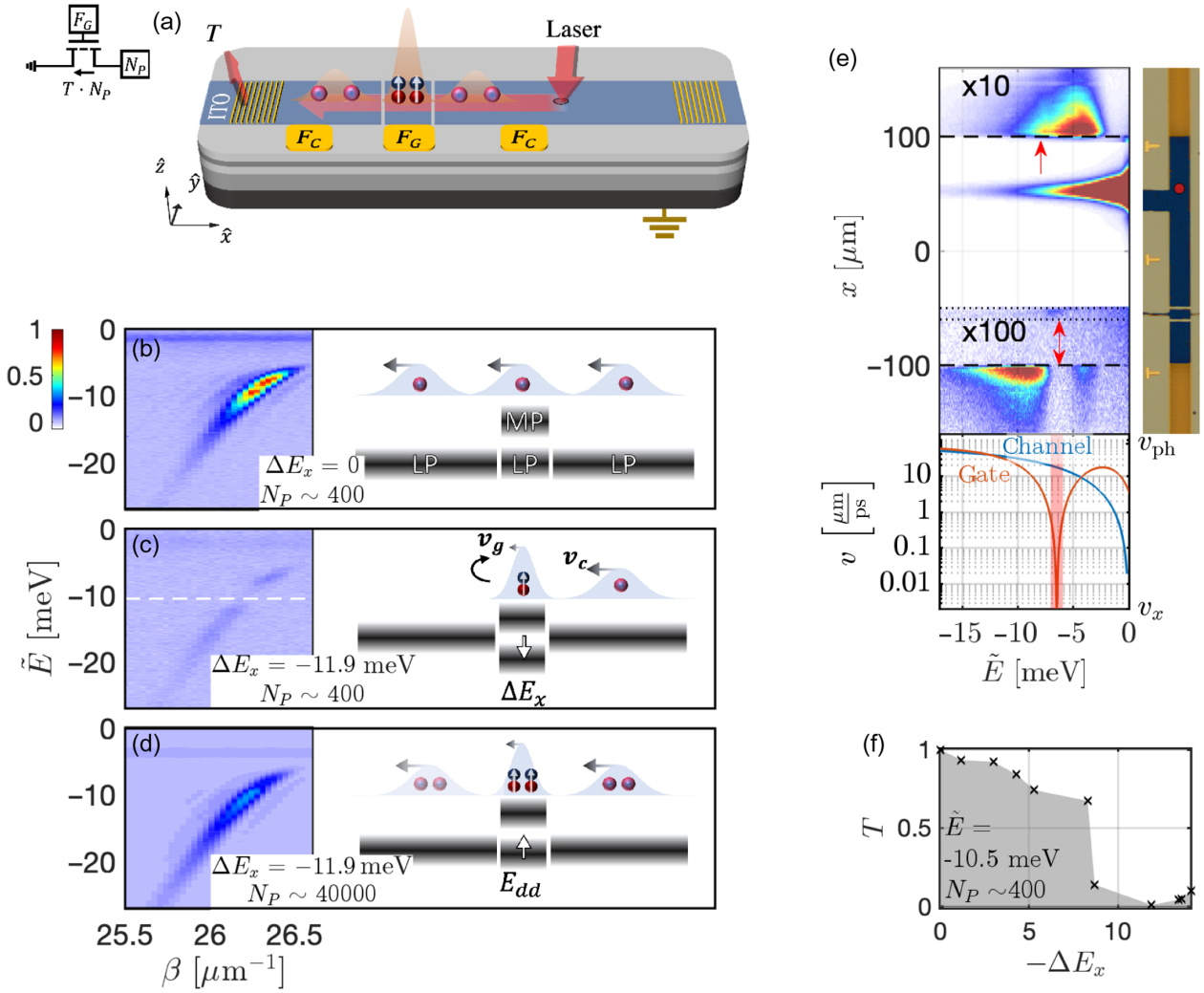

FIG. 3. A dipolariton transistor: strong dipolar interactions of ultraslow polaritons. (a) Illustration of the second device. The principle of operation is described in (b)–(d): (b) Flat potential with a relatively dilute polariton pulse fully transmits; (c) biased gate causes the LP in the channel to overlap mostly with the LP-MP gap in the gate, resulting in a blockage; (d) N_P is increased. This results in a compressed pulse of slow polaritons under the gate. The repulsive dipolar interactions (E_{dd}) induce a blueshift of the dispersion under the gate, enabling transmission. (e) Right: microscope image of the device. The two Au gratings are at the top and the bottom, and the red dot indicates the excitation spot. Left: measured spatially resolved spectrum. Top emission ($x > 100$ μm) of the right movers with a flat potential, bottom emission ($x < -100$ μm) from left movers propagating through a biased gate ($\Delta E_x = -7.5$). The bottom spectrum shows a transmission gap—marked by a double red arrow, which also points to a corresponding emission under the gate at the same energy. The middle ($x \simeq 50$ μm) section shows the emission of the uncoupled exciton under the excitation spot. Attached below is the calculated group velocity [$v_g(\tilde{E})$] of the LP in the channel (blue) and the LP/MP in the gate (red). The red area marks the energy region where $v_g^G \ll v_g^C$, and the gate polaritons become ultraslow. (f) T as a function of $\Delta E_X(F_G)$. The sharp on-off transition of T happens with $\Delta F_G < 0.5$ V/μm.

scattered out of the WG modes through mutual dipolar interactions [27].

Next, we measure the effect of increasing N_P on the transmission. An example is shown in Fig. 3(d) for $N_P \simeq 40\,000$, where the transmission signal recovers almost fully, even at the energies where it was essentially zero at low N_P. This strongly nonlinear transistorlike behavior is explained in the schematics: As N_P increases, the repulsive dipolar interactions of the electrically polarized polaritons penetrating under the gate results in a blueshift $\Delta E_{dd} = g_{dd} \cdot n_G$ of the dipolaritons, where $g_{dd}(F_G)$ is the dipolar interaction constant [27] and n_G is the polariton density under the gate. This interaction-induced blueshift screens the redshift discontinuity ΔE_X, until $\tilde{E}_G(\beta) \simeq \tilde{E}_C(\beta)$. As a result, the electrical blocking is removed, as the interacting dipolaritons overcome the potential well. Importantly, the interaction-induced screening effects with increasing N_P are strongly enhanced not

only by their dipolar nature [24,26–28,31,32,38], but also by the dramatic slowdown of the polaritons under the gate, $v_g^G \ll v_g^C$, resulting in a spatial compression of the polariton pulse, which for a fixed N_P increases n_G compared to n_C:

$$n_G = \int \mathbf{d}E \frac{N_P(E)}{\tau_P w v_g^G(E)}, \tag{1}$$

where w is the effective width of the optical mode in the lateral direction ($\hat{y}$) (more details on this can be found in the SM [40]).

IV. BLOCKADE AND ANTIBLOCKADE OF DIPOLARITONS

Figure 4 demonstrates how our electrically controlled dipolariton transistor can be utilized to display both a polariton blockade and an antiblockade behavior. Figure 4(a) presents schematics of a blockade and an antiblockade. First, the gate is biased such that the MP in the gate overlaps with the LP in the channel and transmits polaritons. Then, N_P is increased, and the slow dipolaritons interact, shifting the states in the gate, such that the LP-MP gap overlaps with the LP branch in the channel, fully blocking transmission. This is the mechanism identified with dipolariton blockade. A further increase of N_P results in an even larger interaction-induced blueshift of the gate, until full transmission is regained via an LP-LP alignment. This part corresponds to an antiblockade process, similar to the facilitation shown for Rydberg atoms [45]. In Fig. 4(b) we plot the transmission spectrum as a function of n_G [bottom x axis; see Eq. (1)] and N_P (top x axis), measured with a constant F_G (corresponding to $\Delta E = -12$ meV at low n_G). Here, we observe a clear blueshift of the LP-MP gap (white line guides the eye) as n_G increases. The blockade or antiblockade mechanism is presented by two fixed energy cross sections of this map (marked by the white dashed lines), plotted in Fig. 4(c): In the top panel, the MP in the gate overlaps with the LP in the channel at low N_P, resulting in a high transmission. When N_P is increased to only ∼1000, the T drops to a minimum, demonstrating a polariton blockade behavior. By further increasing N_P, T rises again, demonstrating an antiblockade behavior. The bottom panel presents a full antiblockade behavior by again increasing N_P to only ∼1000.

Importantly, based on this demonstration, we estimate that both polariton blockade and antiblockade at the quantum level of only two polaritons should be feasible in such a system. This can be seen by setting $N_P = 2$ and choosing a well-defined energy E_P for an injected polariton pulse in Eq. (1). Such substitution simply gives $n_B^G = 2/[\tau_P w v_{\mathrm{ph}} \eta(E_P, F_G)]$, where $\eta = v_g^G(E_p, F_G)/v_{\mathrm{ph}}$. The pulse length τ_P is limited from below by the polariton spectral width γ_P (determined mostly by the excitonic linewidth), $\tau_P > \hbar/\gamma_P$, where in our case $\gamma_P \simeq 0.3$ meV (see Fig. S1 in SM [40]). This limits the polariton pulse duration to be ≥ 2.2 ps. Taking $n_B^G = \Delta n_B$ from Table I, and substituting the values for τ_P, v_{ph} yields a condition on the maximal width of the optical waveguide mode for a true two-polariton blockade:

$$w\eta \leq 4 \times 10^{-3}\ \mu\mathrm{m}. \tag{2}$$

For example, using the extracted value $\eta = 2.5 \times 10^{-3}$ for $\tilde{E} = -9$ meV gives $w \leq 1.5$ μm, a value that should be

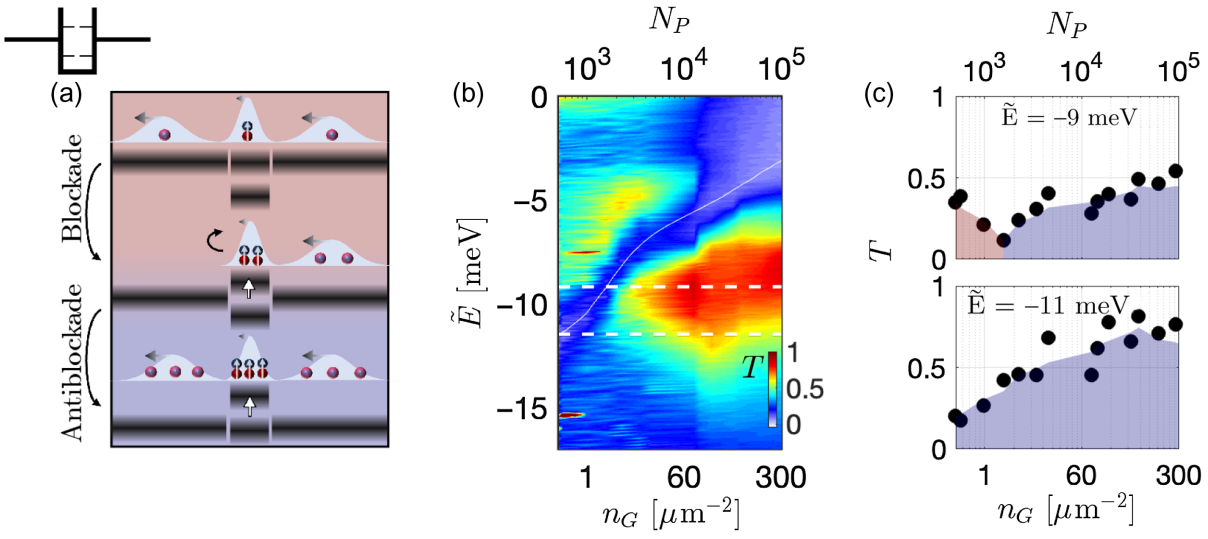

FIG. 4. Blockade and antiblockade of a small number of dipolaritons. (a) Principle of operation of the polariton blockade and antiblockade. (b) Transmission spectrum of the polaritons with a constant gate bias [$\Delta E_X(N_P \to 0) = -11.7$ meV] as a function of the density in the gate n_G (bottom axis), and N_P (top axis). (c) Two slices of the transmission spectrum at $\tilde{E} = -9, -12$ meV, respectively, as a function of N_P (n_G), showing the blockade (pink) and antiblockade (blue) regimes. The slices are marked in (b) by white dashed lines.

TABLE I. Toward a two-dipolariton blockade. The table presents the values extracted from the two transitions described in Fig. 4(c), namely the blockade (B) and antiblockade (AB). ΔN_P and $\Delta n_{\mathrm{B/AB}}$ are the corresponding polaritons number/density difference for blockade/antiblockade, $\tau_p \times w$ are the corresponding values of the pulse duration times the channel width in the current experiment.

	B	AB
$\tilde{E}$	−9	−11 meV
$\Delta n_{\mathrm{B/AB}}$	2.8	5.7 μm^{-2}
ΔN_P	1000	1600
$\tau_p \times w$	1100	1100 μm ps

easily achieved by standard lithography techniques and can safely support guided modes.

While it seems that increasing γ_P allows for shorter pulses and thus higher n_G, we note that it also smears the transmission response to increasing n_B^G and increases the polariton losses; thus it is expected to yield no improvement.

V. LARGE DIPOLAR-INDUCED POLARITON INTERACTIONS: EXPERIMENT AND THEORY

The density-dependent blueshift of the dipolaritons is seen nicely by the shift of the LP-MP gap, marked by a white line in Fig. 4(b). A linear fit to the shift of the gap at low densities $\Delta E_{dd} = g_{dd}(F_G)n_G$ yields a distinctively large $g_{dd}(\Delta E_X = -11.7\ \mathrm{meV}) = 0.7 \pm 0.2\ \mathrm{meV}\,\mu m^2$, a value very similar to our previous results [27], confirming the significant enhancement of dipolariton interactions over nonpolar polaritons or fixed-dipole polaritons [30,31].

To understand and model this large density-dependent polariton blueshift, we suggest a simple dielectric screening model. The dielectric screening induced by the polarized exciton part of the polariton can be presented by an effective density-dependent dielectric constant $\epsilon_{dd}(n_G)$. The dipolar screening reduces the electric field in the QW, as given by (see full derivation in Appendix A)

$$E_G = F_G/\epsilon_{dd}(n_G) = F_G/(1+\chi_{dd}), \tag{3}$$

where

$$\chi_{dd} = \frac{(N_d/V_d)d_X}{\epsilon_0 F_G} = \frac{N_d}{V_d}\frac{\alpha}{\epsilon_0} = \frac{n_G}{L_d}\frac{\alpha}{\epsilon_0}. \tag{4}$$

Here N_d and V_d are the number and volume of the induced excitonic dipoles, $d_X(E_G) = \alpha E_G$, where α is the effective polarizability of an exciton. $L_d(E_G) \approx d_X(E_G)/e$ is the effective dipole layer thickness in the QW quantization direction.

Generally, the energy of free dipoles with a magnitude $d_X = eL_d$ and a density n_G that are introduced into a dielectric medium under a fixed bias V_G is (See Appendix B for full derivation)

$$\Delta E_X(F_G, n_G) = -d_X F_G + \frac{d_X n_G e}{\epsilon_0 \epsilon}, \tag{5}$$

where the first term comes from the dipole-field interaction and the second from the uncorrelated dipole-dipole interaction (known as the plate capacitor formula). Importantly, unlike the case of fixed dipoles, for induced dipoles $d_X = \alpha E_G = \alpha F_G/\epsilon_{dd}(n_G) = \alpha(F_G/1 + \alpha n_G/\epsilon_0 L_d)$, similar to the model in Ref. [27], Eq. (S18), but derived in a different manner. This leads to the following nonlinear density dependent blueshift:

$$\begin{aligned}\Delta E_{dd}(n_G) &= \Delta E_X(F_G, n_G) - \Delta E_X(F_G, 0) \\ &= \alpha F_G^2\left[1 - \left(\frac{1}{(1+\frac{\alpha}{\epsilon_0}n_G/L_d)}\right)\right] \\ &\quad + d\frac{\alpha F_G n_G e}{\epsilon\epsilon_0(1+\frac{\alpha}{\epsilon_0}n_G/L_d)}.\end{aligned} \tag{6}$$

Taking the result up to the first order in n_G, we get

$$\Delta E_{dd}(n_G) \simeq \left(\frac{\alpha^2 F_G^2}{L_d\epsilon_0} + \frac{\alpha F_G e}{\epsilon\epsilon_0}\right)n_G, \tag{7}$$

and we can identify

$$g_{dd} \equiv \frac{\Delta E_{dd}(n_G)}{n_G} \simeq \frac{ed(F_G)}{\epsilon_0}(1 + 1/\epsilon). \tag{8}$$

As can be seen, for induced dipoles, the largest contribution for g_{dd} comes from the density-dependent reduction of d_X, a term which is absent for fixed dipoles.

The only parameter to evaluate in this model is α; this can be done by a numerical solution of $\Delta E_X(F_G)$. To do that we first solve the Schrodinger equation of the wide QW under an applied electric field to find the electron and hole energy shifts and wave functions under an applied field [26,46]. Then, we use a variational method to calculate the changes in binding energy of the exciton under the same field [47,48]. Then $\Delta E_X(F_G, 0)$ is calculated as the sum of the single particle shifts and the change of the exciton binding energy without any fitting parameters. Finally, we set $\alpha = \Delta E_X(F_G, 0)/F_G^2$. A very good agreement was found between the calculated $\Delta E_X(F_G, 0)$ and the experimental results, as shown in Fig. 1(b), yielding

$$\alpha = 1.3\ \frac{\mathrm{meV}}{\mu m^2/V^2}, \tag{9}$$

and therefore we have

$$g_{dd} = 29\ \mu\text{eV}\,\mu\text{m}^2\left(\frac{F_G}{F_G = 1\ \text{V}/\mu\text{m}}\right), \tag{10}$$

which for $F_G = 2.9\ \text{V}/\mu\text{m}$ of Fig. 4 yields $g_{dd} = 84\ \mu\text{eV}\,\mu\text{m}^2$.

The prediction of the model is plotted in Fig. 5(a) together with the extracted ΔE of the LP-MP gap energy from Fig. 4(b). For comparison, the exchange term $g_0 n_G$ is also plotted. The model prediction nicely follows the experimental data and captures the more than an-order-of-magnitude dipolar interaction enhancement over nonpolar polaritons, with no fitting parameters. We note that at low densities, the model prediction is lower than the experimental points [see Fig. 5(b)]. One contribution to the discrepancy may be because our model does not take into account the added screening of the induced polarization field of excitons in all adjacent QWs, which is expected to penetrate all across the sample, as the sample thickness is much smaller than the lateral size of the gate, such that the effective screening field of all the active QWs should be almost additive, $\chi_{dd} \to N_{\text{QW}}\chi_{dd}$, and thus $g_{dd} \to N_{\text{QW}} g_{dd}$. In our structure, 8 QWs are essentially in strong coupling with the WG mode. Setting an effective QW number, $N_{\text{QW}} \simeq 8$, yields $g_{dd} \simeq 0.67\ \text{meV}\,\mu\text{m}^2$, within the uncertainty range of the measurements at very low densities. This is still an open question however.

The effective interaction constant g_{dd} of field-induced dipoles is different from that of fixed dipoles $\tilde{g}_{dd}$, where the latter contains only the screened dipole-dipole interaction term in Eq. (5), and thus yields $\tilde{g}_{dd} = e d_X/\epsilon_0 \epsilon$ [49,50], so

$$g_{dd}/\tilde{g}_{dd} = \epsilon + 1. \tag{11}$$

For GaAs QWs, this ratio is $\epsilon_{\text{GaAs}} + 1 = 13.4$. Figure 5(c) shows the ratio of the field-induced dipole interaction energy of Eq. (6) ΔE_{dd} to that of fixed dipoles $\tilde{\Delta} E_{dd}$, which is significantly larger than 1 over a wide range of densities. This result may explain the mysterious, an-order-of-magnitude discrepancy between the dipolar interaction constant measured for WG dipolaritons with gated wide single GaAs QWs [27,32] and those with asymmetric double GaAs QWs [30,31]. It pinpoints the advantage of using field-induced dipoles for large dipolar nonlinearities, in particular for materials with large dielectric constants. Importantly, this applies also for polaritons based on interlayer excitons in transition metal dichalcogenides heterostructures. It suggests that polaritons based on quadrupolar excitons that were predicted [51] and recently discovered [52–56] may be excellent for nonlinear devices due to their field-induced dipole properties.

Finally, we exclude contributions to the interaction-induced blueshift which are not polaritonic in nature. Since the polaritons are much faster than bare reservoir excitons and free carriers [by order of the mass ratio ($\sim 10^4$)], and since the readout takes place at about 100 μm away from the excitation spot, such a pulsed excitation scheme spatially and temporally separates the polaritons from excitons and other free carriers within each pulse. To prevent pulse-to-pulse memory effects, the repetition rate of the laser was selected to be slower than any long-living charges in the system (SM, Sec. II [40]). Intrapulse exciton accumulation under the gate, where the

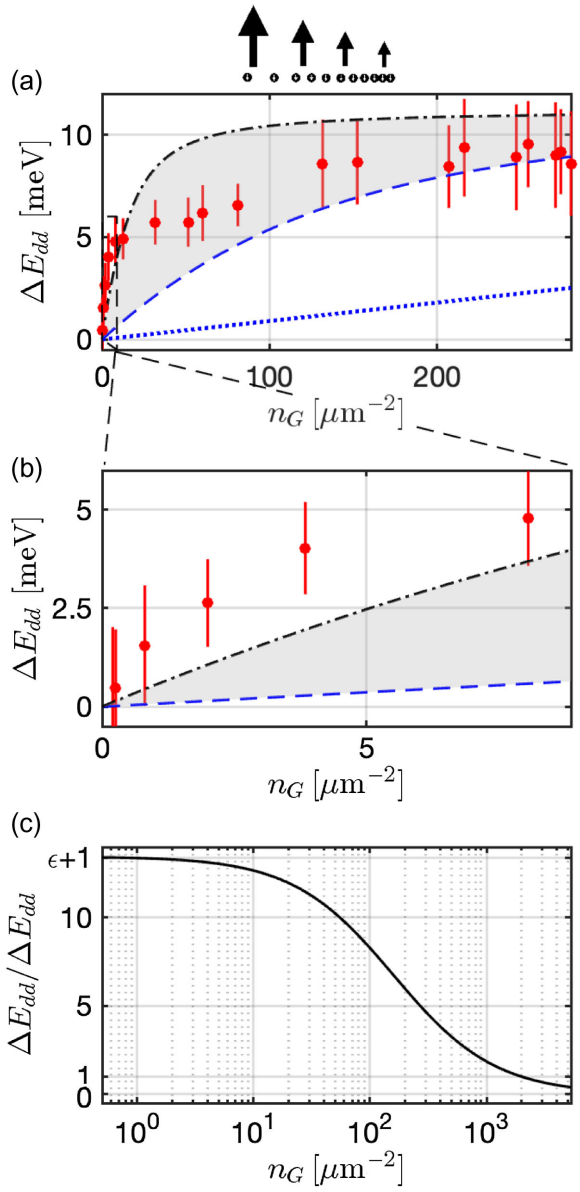

FIG. 5. Field-induced dipolariton interactions. (a) Measured blueshift of the LP-MP gap at the gate (red symbols). The dashed blue line is the prediction of the polarization screening model, Eq. (6) (no fitting parameters). The dot-dashed black line is the prediction for $\chi_{dd} \to N_{\text{QW}}\chi_{dd}$, where $N_{\text{QW}} = 8$. For comparison, the bare contact interaction of nonpolar excitons is shown by the dotted blue line. The errors here are the uncertainty in the middle of the LP-MP gap, the bars show the full width at half the depth. (b) Enlarged view of the low-density regime of (a). (c) The density-dependent interaction-energy blueshift ratio of the field-induced dipoles to that of fixed dipoles.

first polaritons arriving at the gate may disassociate or scatter into excitons that later interact with the rest of the polaritons, can also be excluded: The number of charges is limited by the polaritons failing to transmit through the gate, resulting in low densities over the effective gate area ($\sim 120\ \mu m^2$), which cannot explain the large observed blueshifts at high transmission. We therefore conclude that the observed interactions are very likely polaritonic in nature.

VI. CONCLUSIONS

Strongly interacting gated dipolaritons in wide QWs are a promising platform for the first observation of the long-sought two-polariton blockade, a crucial building block for deterministic quantum photonic integrated circuitry. This demonstration of the fundamental building blocks for electrically controlled photonic logic circuitry in a scalable, planar, on-chip photonic platform approaching the true quantum limit will open up vast opportunities to realize various types of complex photonic processing, either classical or quantum, using dressed dipolar photons.

ACKNOWLEDGMENTS

We thank Eldad Betthelheim and Yoad Ordan for helpful discussions. R. R. and D. L. acknowledge the support from the Israeli Science Foundation Grants No. 836/17 and No. 1087/22, and from the NSF-BSF Grant No. 2019737. J. H., N. L., and H. D. acknowledge the support of the National Science Foundation under Grant No. DMR 2004287, the Air Force Office of Scientific Research under Grant No. FA2386-21-1-4066, and the Gordon and Betty Moore Foundation under Grant No. GBMF10694. The Princeton University portion of this research is funded in part by the Gordon and Betty Moore Foundation's EPiQS Initiative, Grant No. GBMF9615.01 to L. P.

APPENDIX A: INDUCED DIPOLE SCREENING MODEL

From an electrostatic point of view, the sample (see SM for exact details of the sample structure [40]) can be treated as a series of capacitors, each with capacitance c_i; hence, the total capacitance is given by

$$C_{\mathrm{tot}} = \left(\sum_i \frac{1}{c_i}\right)^{-1} = \left(\sum_i \frac{L_i}{A\epsilon_i}\right)^{-1} = A\frac{\prod_i \epsilon_i}{\sum_j L_j \prod_{i\neq j}\epsilon_i}, \tag{A1}$$

where L_i is the thickness of each dielectric layer, ϵ_i is the dielectric constant of each layer, and A is its area. The total capacitance is $Q = CV_0$, where Q is the charge and V_0 the applied bias, and the displacement field between the contacts is $D = Q/A$, the displacement field $D = \epsilon E$ is continuous across the layer boundaries. Using these relations and the above equation, the electric field in the QW is given by

$$E_{\mathrm{QW}} = D/\epsilon_{\mathrm{QW}} = Q/(A\epsilon_{\mathrm{QW}}) = CV_0/(A\epsilon_{\mathrm{QW}}), \tag{A2}$$

$$E_{\mathrm{QW}} = \frac{V_0}{\epsilon_{\mathrm{QW}}}\frac{\prod_i \epsilon_i}{\sum_j L_j \prod_{i\neq j}\epsilon_i}. \tag{A3}$$

Now, when excitons are excited in the QW having a background dielectric constant ϵ_{QW}, the electric field polarizes the excitons, resulting in an additional dipolar screening of the external field $\epsilon_{dd}(n_X)$, with a macroscopic polarization $P_X = \epsilon_0 \chi_{dd} E_{\mathrm{QW}}$. Since $P_X = n_X d_X = n_X \alpha E_{\mathrm{QW}}$, we find

$$\epsilon_{dd}(n_X) = 1 + \chi_{dd}(n_X) = 1 + \frac{n_X \alpha}{\epsilon_0}, \tag{A4}$$

where n_X is an effective three-dimensional density of excitons. This additional screening can be accounted for by replacing ϵ_{QW} by $\epsilon_{\mathrm{QW}} \cdot \epsilon_{dd}$,

$$E_{\mathrm{QW}} = \frac{V_0}{\epsilon_{\mathrm{QW}}\epsilon_{dd}}\frac{\epsilon_{dd}\prod_i \epsilon_i}{\sum_{j\neq \mathrm{QW}} L_j \epsilon_{dd} \prod_{i\neq j}\epsilon_i + L_{\mathrm{QW}} \prod_{i\neq \mathrm{QW}}\epsilon_i}, \tag{A5}$$

$$E_{\mathrm{QW}} = \frac{V_0}{L_{\mathrm{QW}}}\frac{1}{\sum_{j\neq \mathrm{QW}} \frac{L_j}{L_{\mathrm{QW}}}\frac{\prod_{i\neq j}\epsilon_i}{\prod_{i\neq \mathrm{QW}}\epsilon_i}\epsilon_{dd} + 1}, \tag{A6}$$

$$E_{\mathrm{QW}} = \frac{V_0}{L_{\mathrm{QW}}}\frac{1}{\sum_{j\neq \mathrm{QW}} \frac{L_j}{L_{\mathrm{QW}}}\frac{\epsilon_{\mathrm{QW}}}{\epsilon_j}\epsilon_{dd} + 1} \equiv \frac{V_0}{L_{\mathrm{QW}}}\frac{1}{\gamma\epsilon_{dd} + 1}, \tag{A7}$$

where $\gamma \equiv \sum_{j\neq \mathrm{QW}} (L_j/L_{\mathrm{QW}})(\epsilon_{\mathrm{QW}}/\epsilon_j)$ is a property of the structure. Generally, $\gamma \sim L_S/L_{\mathrm{QW}}$, where L_S (L_{QW}) are the widths of the sample and QW, respectively. In our case, therefore, $\gamma \gg 1$. For vanishing dipole density $\epsilon_{dd} \to 1$, and we can define (see Fig. 6)

$$E_{\mathrm{QW}}(n_X = 0) \equiv F_0 = \frac{V_0}{L_{\mathrm{QW}}}\frac{1}{\gamma + 1} \simeq \frac{V_0}{L_S}, \tag{A8}$$

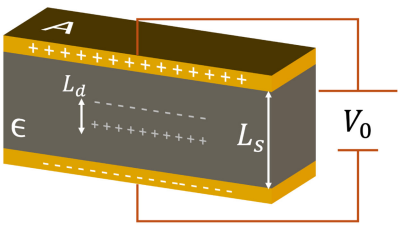

FIG. 6. Plate capacitor screening model: Illustration.

for the sample under study, $F_0 = 0.9(V_0/L_S) = 0.85V_0$ V/μm. Therefore, for a finite dipole density we get

$$E_{\mathrm{QW}}(n_X) = F_0 \frac{\gamma+1}{\epsilon_{dd}\gamma+1} \simeq \frac{F_0}{\epsilon_{dd}} = \frac{F_0}{1+\chi_{dd}}. \quad \text{(A9)}$$

APPENDIX B: INTERACTION-ENERGY SHIFT OF DIPOLAR EXCITONS

The energy of dipoles introduced into an electrically biased dielectric medium ϵ can be calculated as the energy change in the medium when two oppositely charged layers with a separation L_d and total charge Q are inserted into the biased medium. This change is given by [57]

$$\Delta U = \frac{1}{2}\int \mathbf{d}V[E_f \cdot D_f] - \frac{1}{2}\int \mathbf{d}V[E_i \cdot D_i], \quad \text{(B1)}$$

$$\Delta U = \frac{1}{2}\int \mathbf{d}V[E_f \cdot D_f - E_i \cdot D_i], \quad \text{(B2)}$$

where E_i, D_i are the fields without the dipoles and E_f, D_f are with them. The displacement field $D \equiv \epsilon_0\epsilon E$ outside of the inserted charged layers is unchanged while inside it becomes $D_f = D_i - n_{2\mathrm{D}}$, where $n_{2\mathrm{D}} = Q/A$ is the charge density over some area A. Now, we can rewrite the system energy as

$$\Delta U = \frac{1}{2}\int \mathbf{d}V[(E_i - n_{2\mathrm{D}}/\epsilon_0\epsilon)(D_i - n_{2\mathrm{D}}) - E_i \cdot D_i], \quad \text{(B3)}$$

$$\Delta U = \frac{1}{2}\int \mathbf{d}V[-2n_{2\mathrm{D}}E_i + n_{2\mathrm{D}}^2/\epsilon_0\epsilon]; \quad \text{(B4)}$$

integrating the terms gives

$$\Delta U = \frac{1}{2}\int\int \mathbf{d}A\mathbf{d}z[-2Q/AE_i + Q^2/A^2\epsilon_0\epsilon], \quad \text{(B5)}$$

$$\Delta U = \frac{L_d}{2}[2QE_0 - 2Q^2/A\epsilon_0\epsilon], \quad \text{(B6)}$$

$$\Delta U = (QL_d)E_i - (QL_d)(Q/A)/\epsilon_0\epsilon. \quad \text{(B7)}$$

Now, if we define $QL_d = -NeL_d = Nd_X$, we can write the energy per particle:

$$\frac{\Delta U}{N} = -d_X E_i + \frac{d_X n_{2\mathrm{D}} e}{\epsilon_0\epsilon}, \quad \text{(B8)}$$

where e is the elementary charge. The first term is the Stark shift from the dipole-field interaction and the second one is the mean-field, uncorrelated dipole-dipole interaction term (known as the plate capacitor formula); see Refs. [49,50].

Equation (B8) describes the energy either for fixed dipoles ($d_X = d_0$) or for induced dipoles [$d_X = d(E_f)$], where the dipole is a function of the screened electric field E_f (rather than of E_i), which in turn depends on the dipolar density ($n_{2\mathrm{D}}$), as demonstrated in Eq. (A9), $d[E(n_X)] = \alpha E_f(n_X) = \alpha E_i/(1+\chi_{dd})$, where $\chi_{dd} = n_X\alpha/\epsilon_0$, $E_i = F_0 = E_{\mathrm{QW}}(n_X = 0)$, and $E_f = E_{\mathrm{QW}}(n_X)$. As we are interested in a thin layer of dipoles, the density is $n_X = n_{2\mathrm{D}}/L_d$, where $L_d = d_X/e$ is the effective thickness of the layer. Explicitly, the dipolar energies are given by

$$\tilde{U}_{dd} = -d_0 E_i + \frac{d_0 n_{2\mathrm{D}} e}{\epsilon_0\epsilon}, \quad \text{(B9)}$$

$$U_{dd} = -\frac{\alpha E_i}{1+\chi_{dd}}E_i + \frac{\frac{\alpha E_i}{1+\chi_{dd}} n_{2\mathrm{D}} e}{\epsilon_0\epsilon}. \quad \text{(B10)}$$

Here, $\tilde{U}_{dd}$ is the fixed dipole case, and U_{dd} is for induced dipoles. Now if we look at the energy shift as the density grows we can write $\Delta E = U(n) - U(n=0)$:

$$\Delta\tilde{E}_{dd} = \frac{d_0 n_{2\mathrm{D}} e}{\epsilon_0\epsilon}. \quad \text{(B11)}$$

$$\Delta E_{dd} = \alpha E_i^2\left[1 - \frac{1}{1+\chi_{dd}}\right] + \frac{\frac{\alpha E_i}{1+\chi_{dd}} n_{2\mathrm{D}} e}{\epsilon_0\epsilon}. \quad \text{(B12)}$$

Taking this results up to first order in $n_{2\mathrm{D}}$, and substituting $\chi_{dd} = (\alpha n_{2\mathrm{D}}/L_d\epsilon_0)$, gives

$$\Delta\tilde{E}_{dd} = \frac{d_0 e}{\epsilon_0\epsilon} n_{2\mathrm{D}} \quad \text{(B13)}$$

$$\Delta E_{dd} = \left(\frac{\alpha^2 E_i^2}{L_d\epsilon_0} + \frac{\alpha E_i e}{\epsilon_0\epsilon}\right) n_{2\mathrm{D}}. \quad \text{(B14)}$$

We can identify and compare the interaction constants for both cases, $\tilde{g}_{dd}$ g_{dd}, by setting $d_0 = \alpha E_i$ and $L_d = d_0/e$:

$$\tilde{g}_{dd} = \frac{d_0 e}{\epsilon_0\epsilon}, \quad \text{(B15)}$$

$$g_{dd} = \frac{d_0 e}{\epsilon_0}(1 + 1/\epsilon). \quad \text{(B16)}$$

Thus, the ratio of the interaction constant for low densities is given by

$$\frac{g_{dd}}{\tilde{g}_{dd}} = \epsilon + 1. \quad \text{(B17)}$$

For dipoles in vacuum ($\epsilon = 1$), the ratio of the interaction constants is reduced to 2 as expected. This is intuitively

understood as in this case the two terms in Eq. (B13) become equal, and the induced dipole has equal energy contributions from both the dipole-dipole term and the dipole length reduction, while for the fixed dipole only the first term contributes.

[1] Jianwei Wang, Fabio Sciarrino, Anthony Laing, and Mark G. Thompson, *Integrated photonic quantum technologies*,. Nat. Photonics **14**, 273 (2019).

[2] Ali W. Elshaari, Wolfram Pernice, Kartik Srinivasan, Oliver Benson, and Val Zwiller, *Hybrid integrated quantum photonic circuits*, Nat. Photonics **14**, 285 (2020).

[3] Wim Bogaerts, Daniel Pérez, José Capmany, David A. B. Miller, Joyce Poon, Dirk Englund, Francesco Morichetti, and Andrea Melloni, *Programmable photonic circuits*, Nature (London) **586**, 207 (2020).

[4] L. V. Butov, *Excitonic devices*, Superlattices Microstruct. **108**, 2 (2017).

[5] Alberto Ciarrocchi, Fedele Tagarelli, Ahmet Avsar, and Andras Kis, *Excitonic devices with van der Waals heterostructures: Valleytronics meets twistronics*, Nat. Rev. Mater. **7**, 449 (2022).

[6] S. Lazić, A. Violante, K. Cohen, R. Hey, R. Rapaport, and P. V. Santos, *Scalable interconnections for remote indirect exciton systems based on acoustic transport*, Phys. Rev. B **89**, 085313 (2014).

[7] Alex A. High, Ekaterina E. Novitskaya, Leonid V. Butov, Micah Hanson, and Arthur C. Gossard, *Control of exciton fluxes in an excitonic integrated circuit*, Science **321**, 229 (2008).

[8] Hui Deng, Hartmut Haug, and Yoshihisa Yamamoto, *Exciton-polariton Bose-Einstein condensation*, Rev. Mod. Phys. **82**, 1489 (2010).

[9] Daniele Sanvitto and Stéphane Kéna-Cohen, *The road towards polaritonic devices*, Nat. Mater. **15**, 1061 (2016).

[10] D. E. Chang, J. S. Douglas, A. González-Tudela, C. L. Hung, and H. J. Kimble, *Colloquium: Quantum matter built from nanoscopic lattices of atoms and photons*, Rev. Mod. Phys. **90**, 031002 (2018).

[11] Thibault Peyronel, Ofer Firstenberg, Qi Yu Liang, Sebastian Hofferberth, Alexey V. Gorshkov, Thomas Pohl, Mikhail D. Lukin, and Vladan Vuletić, *Quantum nonlinear optics with single photons enabled by strongly interacting atoms*, Nature (London) **488**, 57 (2012).

[12] Daniel Tiarks, Steffen Schmidt-Eberle, Thomas Stolz, Gerhard Rempe, and Stephan Dürr, *A photon-photon quantum gate based on Rydberg interactions*, Nat. Phys. **15**, 124 (2018).

[13] Jianbo De, Xuekai Ma, Fan Yin, Jiahuan Ren, Jiannian Yao, Stefan Schumacher, Qing Liao, Hongbing Fu, Guillaume Malpuech, and Dmitry Solnyshkov, *Room-temperature electrical field-enhanced ultrafast switch in organic microcavity polariton condensates*, J. Am. Chem. Soc. **145**, 1557 (2023).

[14] Anton V. Zasedatelev, Anton V. Baranikov, Denis Sannikov, Darius Urbonas, Fabio Scafirimuto, Vladislav Yu Shishkov, Evgeny S. Andrianov, Yurii E. Lozovik, Ullrich Scherf, Thilo Stöferle, Rainer F. Mahrt, and Pavlos G. Lagoudakis, *Single-photon nonlinearity at room temperature*, Nature (London) **597**, 493 (2021).

[15] A. Amo, T. C. H. Liew, C. Adrados, R. Houdré, E. Giacobino, A. V. Kavokin, and A. Bramati, *Exciton-polariton spin switches*, Nat. Photonics **4**, 361 (2010).

[16] Félix Marsault, Hai Son Nguyen, Dimitrii Tanese, Aristide Lemaître, Elisabeth Galopin, Isabelle Sagnes, Alberto Amo, and Jacqueline Bloch, *Realization of an all optical exciton-polariton router*, Appl. Phys. Lett. **107**, 201115 (2015).

[17] H. S. Nguyen, D. Vishnevsky, C. Sturm, D. Tanese, D. Solnyshkov, E. Galopin, A. Lemaître, I. Sagnes, A. Amo, G. Malpuech, and J. Bloch, *Realization of a double-barrier resonant tunneling diode for cavity polaritons*, Phys. Rev. Lett. **110**, 236601 (2013).

[18] T. Gao, P. S. Eldridge, T. C. H. Liew, S. I. Tsintzos, G. Stavrinidis, G. Deligeorgis, Z. Hatzopoulos, and P. G. Savvidis, *Polariton condensate transistor switch*, Phys. Rev. B **85**, 235102 (2012).

[19] D. Ballarini, M. De Giorgi, E. Cancellieri, R. Houdré, E. Giacobino, R. Cingolani, A. Bramati, G. Gigli, and D. Sanvitto, *All-optical polariton transistor*, Nat. Commun. **4**, 1778 (2013).

[20] H. Suchomel, S. Brodbeck, T. C. H. Liew, M. Amthor, M. Klaas, S. Klembt, M. Kamp, S. Höfling, and C. Schneider, *Prototype of a bistable polariton field-effect transistor switch*, Sci. Rep. **7**, 5114 (2017).

[21] Aymeric Delteil, Thomas Fink, Anne Schade, Sven Höfling, Christian Schneider, and Ataç İmamoğlu, *Towards polariton blockade of confined exciton–polaritons*, Nat. Mater. **18**, 219 (2019).

[22] Guillermo Muñoz-Matutano, Andrew Wood, Mattias Johnsson, Xavier Vidal, Ben Q. Baragiola, Andreas Reinhard, Aristide Lemaître, Jacqueline Bloch, Alberto Amo, Gilles Nogues, Benjamin Besga, Maxime Richard, and Thomas Volz, *Emergence of quantum correlations from interacting fibre-cavity polaritons*, Nat. Mater. **18**, 213 (2019).

[23] Yongbao Sun, Yoseob Yoon, Mark Steger, Gangqiang Liu, Loren N. Pfeiffer, Ken West, David W. Snoke, and Keith A. Nelson, *Direct measurement of polariton-polariton interaction strength*, Nat. Phys. **13**, 870 (2017).

[24] D. W. Snoke, V. Hartwell, J. Beaumariage, S. Mukherjee, Y. Yoon, D. M. Myers, M. Steger, Z. Sun, K. A. Nelson, and L. N. Pfeiffer, *Reanalysis of experimental determinations of polariton-polariton interactions in microcavities*, Phys. Rev. B **107**, 165302 (2023).

[25] M. Vladimirova, S. Cronenberger, D. Scalbert, K. V. Kavokin, A. Miard, A. Lemaître, J. Bloch, D. Solnyshkov, G. Malpuech, and A. V. Kavokin, *Polariton-polariton interaction constants in microcavities*, Phys. Rev. B **82**, 075301 (2010).

[26] Itamar Rosenberg, Yotam Mazuz-Harpaz, Ronen Rapaport, Kenneth West, and Loren Pfeiffer, *Electrically controlled mutual interactions of flying waveguide dipolaritons*, Phys. Rev. B **93**, 195151 (2016).

[27] Itamar Rosenberg, Dror Liran, Yotam Mazuz-Harpaz, Kenneth West, Loren Pfeiffer, and Ronen Rapaport, *Strongly interacting dipolar-polaritons*, Sci. Adv. **4**, eaat8880 (2018).

[28] D. G. Suárez-Forero, F. Riminucci, V. Ardizzone, N. Karpowicz, E. Maggiolini, G. Macorini, G. Lerario, F. Todisco, M. De Giorgi, L. Dominici, D. Ballarini, G. Gigli, A. S. Lanotte, K. West, K. Baldwin, L. Pfeiffer, and D. Sanvitto, *Enhancement of parametric effects in polariton waveguides induced by dipolar interactions*, Phys. Rev. Lett. **126**, 137401 (2021).

[29] S. I. Tsintzos, A. Tzimis, G. Stavrinidis, A. Trifonov, Z. Hatzopoulos, J. J. Baumberg, H. Ohadi, and P. G. Savvidis, *Electrical tuning of nonlinearities in exciton-polariton condensates*, Phys. Rev. Lett. **121**, 037401 (2018).

[30] Peter Cristofolini, Gabriel Christmann, Simeon I. Tsintzos, George Deligeorgis, George Konstantinidis, Zacharias Hatzopoulos, Pavlos G. Savvidis, and Jeremy J. Baumberg, *Coupling quantum tunneling with cavity photons*, Science **336**, 704 (2012).

[31] Emre Togan, Hyang Tag Lim, Stefan Faelt, Werner Wegscheider, and Atac Imamoglu, *Enhanced interactions between dipolar polaritons*, Phys. Rev. Lett. **121**, 227402 (2018).

[32] Biswajit Datta, Mandeep Khatoniar, Prathmesh Deshmukh, Félix Thouin, Rezlind Bushati, Simone De Liberato, Stephane Kena Cohen, and Vinod M. Menon, *Highly nonlinear dipolar exciton-polaritons in bilayer* MoS_2, Nat. Commun. **13**, 1 (2022).

[33] P. M. Walker, L. Tinkler, B. Royall, D. V. Skryabin, I. Farrer, D. A. Ritchie, M. S. Skolnick, and D. N. Krizhanovskii, *Dark solitons in high velocity waveguide polariton fluids*, Phys. Rev. Lett. **119**, 097403 (2017).

[34] Dror Liran, Itamar Rosenberg, Ken West, Loren Pfeiffer, and Ronen Rapaport, *Fully guided electrically controlled exciton polaritons*, ACS Photonics **5**, 4249 (2018).

[35] C. Brimont, L. Doyennette, G. Kreyder, F. Réveret, P. Disseix, F. Médard, J. Leymarie, E. Cambril, S. Bouchoule, M. Gromovyi, B. Alloing, S. Rennesson, F. Semond, J. Zúñiga-Pérez, and T. Guillet, *Strong coupling of exciton-polaritons in a bulk* GaN *planar waveguide: Quantifying the coupling strength*, Phys. Rev. Appl. **14**, 054060 (2020).

[36] D. G. Suárez-Forero, F. Riminucci, F. Riminucci, V. Ardizzone, M. De Giorgi, L. Dominici, F. Todisco, G. Lerario, L. N. Pfeiffer, G. Gigli, D. Ballarini, D. Sanvitto, and D. Sanvitto, *Electrically controlled waveguide polariton laser*, Optica **7**, 1579 (2020).

[37] Davide Nigro, Vincenzo D'Ambrosio, Daniele Sanvitto, and Dario Gerace, *Integrated quantum polariton interferometry*, Commun. Phys. **5**, 34 (2022).

[38] Esben R. Christensen, Arturo Camacho-Guardian, Ovidiu Cotlet, Atac Imamoglu, Michiel Wouters, Georg M. Bruun, and Iacopo Carusotto, *Microscopic theory of cavity-enhanced interactions of dipolaritons*, arXiv:2212.02597v1.

[39] Haonan Ling, Arnab Manna, Jialiang Shen, Ho-Ting Tung, David Sharp, Johannes Fröch, Johannes Fröch, Siyuan Dai, Siyuan Dai, Arka Majumdar, Arka Majumdar, Arka Majumdar, and Artur R. Davoyan, *Deeply subwavelength integrated excitonic van der Waals nanophotonics*, Optica **10**, 1345 (2023).

[40] See Supplemental Material at http://link.aps.org/supplemental/10.1103/PhysRevX.14.031022 for a detailed description of the sample, calibration of the experimental setup, and characterization of the polariton devices under study, which includes Refs. [41–44].

[41] *Confined Electrons and Photons*, Elias Burstein and Claude Weisbuch, NATO ASI Vol. 340 (Springer, Boston, MA, 1995).

[42] Ruzi Mahmut, *Voigt line shape fit, File exchange, MATLAB central*, 2023, https://www.mathworks.com/matlabcentral/fileexchange/57603-voigt-line-shape-fit.

[43] *Table of refractive index values for thin film thickness measurement*, https://www.filmetrics.com/refractive-index-database.

[44] Rita Claudia Iotti and Lucio Claudio Andreani, *Crossover from strong to weak confinement for excitons in shallow or narrow quantum wells*, Phys. Rev. B **56**, 3922 (1997).

[45] Matteo Marcuzzi, Jiří Minář, Daniel Barredo, Sylvain De Léséleuc, Henning Labuhn, Thierry Lahaye, Antoine Browaeys, Emanuele Levi, and Igor Lesanovsky, *Facilitation dynamics and localization phenomena in Rydberg lattice gases with position disorder*, Phys. Rev. Lett. **118**, 063606 (2017).

[46] Yotam Mazuz-Harpaz, Kobi Cohen, Boris Laikhtman, Ronen Rapaport, Ken West, and Loren N. Pfeiffer, *Radiative lifetimes of dipolar excitons in double quantum wells*, Phys. Rev. B **95**, 155302 (2017).

[47] D. A. B. Miller, D. S. Chemla, T. C. Damen, A. C. Gossard, W. Wiegmann, T. H. Wood, and C. A. Burrus, *Band-edge electroabsorption in quantum well structures: The quantum-confined Stark effect*, Phys. Rev. Lett. **53**, 2173 (1984).

[48] G. Bastard, Wave Mechanics Applied to Semiconductor Heterostructures, Les Editions de Physique, 1988, ISBN 2868830927.

[49] B. Laikhtman and R. Rapaport, *Exciton correlations in coupled quantum wells and their luminescence blue shift*, Phys. Rev. B **80**, 195313 (2009).

[50] B. Laikhtman and R. Rapaport, *Correlations in a two-dimensional Bose gas with long-range interaction*, Europhys. Lett. **87**, 27010 (2009).

[51] Yevgeny Slobodkin, Yotam Mazuz-Harpaz, Sivan Refaely-Abramson, Snir Gazit, Hadar Steinberg, and Ronen Rapaport, *Quantum phase transitions of trilayer excitons in atomically thin heterostructures*, Phys. Rev. Lett. **125**, 255301 (2020).

[52] Weijie Li, Zach Hadjri, Luka M. Devenica, Jin Zhang, Song Liu, James Hone, Kenji Watanabe, Takashi Taniguchi, Angel Rubio, and Ajit Srivastava, *Quadrupolar–dipolar excitonic transition in a tunnel-coupled van der Waals heterotrilayer*, Nat. Mater. **22**, 1478 (2023).

[53] Leo Yu, Kateryna Pistunova, Jenny Hu, Kenji Watanabe, Takashi Taniguchi, and Tony F. Heinz, *Observation of quadrupolar and dipolar excitons in a semiconductor heterotrilayer*, Nat. Mater. **22**, 1485 (2023).

[54] Yongzhi Xie, Yuchen Gao, Fengyu Chen, Yunkun Wang, Jun Mao, Qinyun Liu, Saisai Chu, Hong Yang, Yu Ye, Qihuang Gong, Ji Feng, and Yunan Gao, *Bright and dark quadrupolar excitons in the* $WSe_2/MoSe_2/WSe_2$ *heterotrilayer*, Phys. Rev. Lett. **131**, 186901 (2023).

[55] Zhen Lian, Dongxue Chen, Lei Ma, Yuze Meng, Ying Su, Li Yan, Xiong Huang, Qiran Wu, Xinyue Chen, Mark Blei, Takashi Taniguchi, Kenji Watanabe, Sefaattin Tongay, Chuanwei Zhang, Yong Tao Cui, and Su Fei Shi, *Quadrupolar excitons and hybridized interlayer Mott insulator in a trilayer moiré superlattice*, Nat. Commun. **14**, 1 (2023).

[56] Yusong Bai, Yiliu Li, Song Liu, Yinjie Guo, Jordan Pack, Jue Wang, Cory R. Dean, James Hone, and Xiaoyang Zhu, *Evidence for exciton crystals in a 2D semiconductor heterotrilayer*, Nano Lett. **23**, 11621 (2023).

[57] John David Jackson, *Classical Electrodynamics*, 3rd ed. (Wiley, New York, 1999).